

# Reversal of chronic surface degradation of Sr(Ti,Fe)O<sub>3</sub> perovskite-based fuel cell cathodes by surface acid/base engineering

Han Gil Seo <sup>a,b,\*</sup>, Hyunseung Kim <sup>c</sup>, WooChul Jung <sup>c</sup>, Harry L. Tuller <sup>a,\*</sup>

<sup>a</sup> Department of Materials Science and Engineering, Massachusetts Institute of Technology, Cambridge, MA 02139, USA

<sup>b</sup> Department of Materials Science and Engineering, Dankook University, 119 Dandae-ro, Dongnam-gu, Cheonan-si, Chungnam 31116, Republic of Korea

<sup>c</sup> Department of Materials Science and Engineering, Korea Advanced Institute of Science and Technology, Daejeon 34141, Republic of Korea



## ARTICLE INFO

### Keywords:

Surface degradation  
Co-free perovskite cathode  
Oxygen-reduction reaction  
Acid/base engineering

## ABSTRACT

The major barrier to commercialization of solid oxide fuel cells (SOFCs) is to overcome long-term surface degradation during operation. Sr/Co-based perovskite cathodes have been recognized to suffer from two major sources of degradation: inherent Sr segregation and extrinsic Cr-impurities at the surface, respectively. Here, we demonstrate the ability to simultaneously reverse both surface degradation modes in SrTi<sub>0.65</sub>Fe<sub>0.35</sub>O<sub>3-δ</sub> (STF35), a model high performance perovskite cathode, via surface acid/base engineering via infiltration. The acidic nature of Cr-infiltration is found to induce surface electron depletion, while enhancing Sr segregation to the surface, leading to ~40% drop in SOFC peak power. Subsequent infiltration of basic Ca-additives is demonstrated to not only neutralize these detrimental effects, but ultimately lead to 160% enhancement in peak power, thereby enabling Co-free operation. This approach holds great promise for extending the operating lives, more generally, of materials and devices for which the catalytic oxygen/solid interface reaction is central.

## 1. Introduction

Various energy-related technologies depend heavily on the conduction of both ions and electrons, as well as the interaction of surfaces with atmospheric oxygen. These technologies encompass a wide range of devices for energy conversion and storage, such as solid oxide fuel/electrolysis cells (SOFCs/SOECs) [1,2], oxygen permeation membranes [3,4], solar thermochemical fuel production [5,6], automotive emission catalysts [7], and metal oxide-based gas sensors [8,9]. The efficient functioning of many of these devices hinges on swift oxygen exchange reactions occurring at the interfaces between the respective gases and solids. For instance, in intermediate-temperature SOFCs, the oxygen reduction reaction (ORR) at the cathode plays a pivotal role in determining the overall polarization resistance due to its considerable overpotential [10]. Despite numerous endeavors aimed at enhancing the initial ORR activity, particularly concentrating on mixed conducting Co-based perovskite oxides [11–13], the surfaces of these materials inevitably suffer from poisoning over time during device operation. Consequently, this leads to unacceptable levels of performance degradation and diminished lifetimes of the devices [14–16].

Cathode materials, most commonly characterized by the perovskite crystal structure, characterized by the general formula ABO<sub>3</sub>, and exhibiting high mixed ionic and electronic conductivities (MIEC), including (La,Sr)CoO<sub>3</sub> (LSC) [17,18], (La,Sr)(Co,Fe)O<sub>3</sub> (LSCF) [19], Sr(Ti,Fe)O<sub>3</sub> (STF) [20], (Sm,Sr)CoO<sub>3</sub> (SSC) [12], (Ba,Sr)(Co,Fe)O<sub>3</sub> (BSCF) [21], Sr(Y,Nb,Co)O<sub>3-δ</sub> [1], and (Pr,Nd)(Ba,Ca,Sr)(Co,Fe)<sub>2</sub>O<sub>5+δ</sub> [22], have long been explored due to their impressive ORR activity at intermediate temperatures. However, these materials encounter surface degradation in their ORR kinetics stemming from both intrinsic and extrinsic sources. Intrinsic degradation often arises from the migration of large cations from the A site within ABO<sub>3</sub> to the surface, resulting in, for example enrichment of SrO or BaO. Conversely, extrinsic degradation involves the accumulation of poisons, primarily vaporized Cr- or Si-based species, on the perovskite surface during practical operation of SOFCs. These poisons typically originate from the Cr-based metal interconnects (e.g. Crofer 22 APU and SUS430) [23] and furnace refractories/ceramic sealants [16] respectively, utilized in commercial SOFC systems.

Traditional high-temperature alloy interconnects typically incorporate chromium for the purpose of enhancing resistance against corrosion

\* Corresponding author at: Department of Materials Science and Engineering, Dankook University, 119 Dandae-ro, Dongnam-gu, Cheonan-si, Chungnam 31116, Republic of Korea.

\*\* Corresponding author.

E-mail addresses: [hgseo89@dankook.ac.kr](mailto:hgseo89@dankook.ac.kr) (H.G. Seo), [hltuller@mit.edu](mailto:hltuller@mit.edu) (H.L. Tuller).

and oxidation. However, the vaporized chromium species such as  $\text{CrO}_2(\text{OH})_2(\text{g})$  and  $\text{CrO}_3(\text{g})$  are observed to travel onto the cathode surface under device operation, forming  $\text{Cr}_2\text{O}_3(\text{s})$  or secondary Cr-compounds formed by reaction with segregated Sr (e.g. strontium chromate) [24,25]. Since both are electronically and ionically insulating, they ultimately result in performance degradation. Several strategies to mitigate chrome's detrimental effects were investigated including by (i) use of Cr-getters [26], (ii) coating of the interconnects [27], and (iii) surface modifications with demonstrated high resistance to Cr-poisoning [28–30]. For example, Hong et al., captured gaseous Cr-species by using a strontium nickel oxide getter [26] while Park et al., introduced a conformal bi-layered perovskite/spinel coating via electrodeposition to stabilize the Crofer surface [27]. In addition, Niu et al., improved the performance and tolerance of LSCF cathodes to Cr-poisoning by application of a multiphase catalyst coating [28]. Nevertheless, a systematic understanding of Cr-poisoning behavior on perovskite cathodes remains elusive.

Meanwhile, while surface segregated alkaline earth oxides, notably  $\text{SrO}_x$ , are nearly universally viewed as detrimental to fuel cell cathode performance, by serving as a charge-transfer barrier for ORR activity [31–33], there are scattered references in the literature that report that  $\text{SrO}$  deposited onto perovskite surfaces can instead lead to ORR activity enhancement [33–39]. We begin by listing a few representative examples of the former. Rupp et al. examined the effect of cation-additives (e.g.  $\text{SrO}$ ,  $\text{Co}_3\text{O}_4$ , and  $\text{La}_2\text{O}_3$ ) from an external source on the ORR activity of LSC electrodes with the aid of in-situ surface modification by pulsed laser deposition (PLD), and concluded that  $\text{SrO}$  decoration led to a rapid drop in ORR activity [34]. Jung et al. reported that while segregated  $\text{Sr}$ -excess in the form of Ruddlesden-Popper phases, or  $\text{SrO}$  island precipitates on STF thin film surfaces, are found to degrade performance, the surface ORR activity could be reactivated by etching away the  $\text{Sr}$ -excess layers [33]. A recent review by Safian et al., summarizes the extensive literature on the negative impact of surface segregation of  $\text{Sr}$  on the performance of MIEC lanthanum-based perovskite oxide LSCF cathode materials [40]. Although many fewer in number, there are some reports of the reverse effect. For example, Mutoro et al. reported that PLD-driven surface decoration with  $\text{Sr}$  accelerated the surface oxygen exchange kinetics of an LSC thin film electrode by a factor of ten [35]. Similarly, Wagner and Argirisus et al. demonstrated the ability of alkaline earth (Ca, Sr, Ba) metal oxides to promote the exchange rate of oxygen of both undoped and Fe-doped  $\text{SrTiO}_3$  bulk polycrystalline materials [36–38]. Siebenhofer et al., in a recent report, indicated two opposite impacts on the ORR activity of  $\text{Sr}$ -decorated LSC thin films depending on environmental conditions (i.e. temperature and oxygen partial pressure), i.e., while the formation of  $\text{SrO}$  deposited at high temperatures improved the electrochemical performance,  $\text{SrCO}_3$  adsorbates formed by reaction with  $\text{CO}_2$  gases during low-temperature deposition deactivated the rate of oxygen exchange [39]. They also agreed that the ionic potential of surface cations, and their corresponding acid/base character, can serve as a readily accessible descriptor for oxygen exchange kinetics by tailoring the surface dipole and work function [41]. In the present study, we demonstrate how these apparent discrepancies in the literature can be explained and indeed how carefully controlled additions of alkaline earth oxides, and other oxides with high basicity, can be used to markedly enhance oxygen exchange kinetics at MIEC metal oxide perovskite surfaces and/or recover the performance of such electrodes following degradation in performance by the well-known chromia-based poison sourced from metallic SOFC interconnects [23].

Recent publications have highlighted the significance of the relative acidity of binary oxides as a crucial factor in determining the oxygen exchange kinetics of MIEC oxides [42–44]. Through the use of various surface additives, studies on an alternative model fluorite-structured  $\text{Pr}_{0.1}\text{Ce}_{0.9}\text{O}_{2-\delta}$  (PCO) MIEC porous cathode material have demonstrated remarkable variations, of up to six orders of magnitude, in the surface oxygen exchange coefficient ( $k_{\text{chem}}$ ) [42]. Initially, the choice of PCO

aimed to simplify the interpretation by avoiding complexities associated with  $\text{Sr}$  segregation observed in perovskite oxides, as mentioned earlier. The notable variations in  $k_{\text{chem}}$  were attributed to electronic interactions at the interfaces between the additives and PCO, resulting in the surface depletion (or accumulation) of electrons by acidic (or basic) additives, thereby leading to corresponding decreases (or increases) in  $k_{\text{chem}}$  [42]. Building on this understanding, efforts were directed towards mitigating the adverse effects of acidic species from external sources, viz. Cr- and Si- species, on the ORR at PCO surfaces by introducing more basic species like  $\text{Li}_2\text{O}$  or  $\text{CaO}$  [43,44]. With the successful completion of these studies, there is a pressing need to further validate the broader applicability of our acid/base model in predicting the inhibition or enhancement of oxygen exchange kinetics, particularly focusing on the technically relevant, yet more complex perovskite MIECs.

Accordingly, we focus our attention on a MIEC perovskite material. We selected a member of the  $\text{Sr}(\text{Tl}_{1-x}\text{Fe}_x)\text{O}_3$  (STF) system, namely  $\text{Sr}(\text{Ti}_{0.65}\text{Fe}_{0.35})\text{O}_3$  (STF35), rather than say LSCF for a number reasons. First, the A site in perovskite STF (general formula  $\text{ABO}_3$ ) is occupied by only  $\text{Sr}$ , eliminating the need to be concerned about the relative ratio of La/Sr both within the bulk of the material and in the vicinity of the surface [45]. Nevertheless, like many of the most promising perovskites listed above, STF is well known to exhibit  $\text{Sr}$  segregation towards the surface during operation, leading to performance degradation [33,46]. The driving forces for  $\text{Sr}$  segregation in STF have also been examined in some detail, including electrostatic and strain effects, as well as tactics that could potentially be used to minimize segregation [31,46,47]. Second, as the authors have demonstrated in the past, the system is highly versatile in that the STF system remains stable within the perovskite phase across the full composition range between the  $\text{SrTiO}_3$  and  $\text{SrFeO}_3$  end members under both reducing and oxidizing atmospheres. This allows one to tune both the oxygen ionic and electronic conductivities ranging from insulating for the  $\text{SrTiO}_3$  end member to metallic and fast ion conducting for the  $\text{SrFeO}_3$  end member [48], leading to reported utilization of STF as both SOFC anode [49–51] and cathode [13,20,52]. Furthermore, the authors also previously demonstrated that there was a close correlation between the position of the Fermi energy relative to the conduction band edge and the activation energy associated with the ORR activity [20]. This strongly suggested that minority electrons, rather than majority holes in STF, control the charge transfer reaction. This feature, as we will demonstrate shortly, is central to the acid/base theory mentioned above. Finally, it should be noted that in contrast to nearly all the other examples of MIECs that are utilized as highly performing cathode materials (see above), STF does not contain Co. Co is both more costly than Fe, as well as being viewed as a critical material, given its near universal use in lithium battery cathodes that in coming years is expected to grow by orders of magnitude as internal combustion vehicles are rapidly replaced by electric vehicles [53]. Thus, finding an effective Co-free substitute like STF has great value. Indeed, Zhang et al. reported that STF exhibited comparable, if not better, initial performance than LSCF, coupled with much improved long term stability (note: optimum performance in that study achieved upon substitution of 15% of Co for Fe in  $\text{Sr}(\text{Ti}_{0.3}\text{Fe}_{0.7})\text{O}_3$ ) [13]. Furthermore, it should be noted that the STF system has already been examined in terms of its defect, transport,  $\text{Sr}$  segregation, and surface reaction characteristics [20,33,48]. As a consequence, the perovskite-structured STF oxide serves as a particularly good candidate cathode for study in that it not only serves as a practical example of a perovskite cathode material with superior performance, but also from a model standpoint, being amenable for illustrating the ability of our acid/base model to demonstrate acidic-poisoning and basic-recovery of surface additives. This ultimately, as we demonstrate below, holds great import for future improved fuel cell performance and lifetimes.

In this work, we demonstrate how surface degradation of fuel cell performance utilizing a STF35 cathode is completely reversed with appropriately controlled surface acidity. We systematically examine the effects of extrinsic Cr- or Ca-based surface additives on (1)  $k_{\text{chem}}$  by

conductivity relaxation experiments, (2) the ASR of symmetric cells by electrochemical impedance measurements (EIS), and (3) the power output of a single cell fuel cell by current( $I$ )-voltage( $V$ ) measurements. Cr-additives lead to remarkable depressions in  $k_{chem}$ , increases in ASR, and depressions in peak power density by over 100-fold, 10-fold, and  $\sim 40\%$  respectively due to its acidic nature relative to that of STF. When subsequent infiltration with basic Ca-additives is applied onto the Cr-poisoned STF electrode, full recovery of performance degradation in all those metrics is obtained, together with long-term stability by scavenging and neutralizing Cr-poison species. Surface acid/base engineering, as employed here, can therefore be an exceptionally efficient route, not only for refreshing degraded device performance, but also for designing highly active electrode surfaces tuned by the relative acidity of additives with high tolerance against various external poisoning sources. This approach should apply as well in other technologies in which the gas/solid interface plays a central role, ranging from fuel/electrolysis cells to permeation membranes, sensors, and catalysts.

## 2. Experimental

### 2.1. Fabrication of porous STF35 bulk ceramics

$\text{SrTi}_{0.65}\text{Fe}_{0.35}\text{O}_{3-\delta}$  (STF35) powder was synthesized by a conventional solid-state reaction, using strontium carbonate ( $\text{SrCO}_3$ , Alfa Aesar, 99.99%), titanium (IV) oxide ( $\text{TiO}_2$ , Alfa Aesar, 99.9%), and iron (III) oxide ( $\text{Fe}_2\text{O}_3$ , Alfa Aesar, 99.9%) powders. The powders were mixed to obtain the desired Sr:Ti:Fe stoichiometric ratios, and ball milled with ethanol for 24 h. The resulting powders were dried on a hot plate and in an oven, and then subsequently calcined at 1000 °C for 12 h in ambient air at a heating/cooling rate of 5 °C/min. The calcined powders were then lightly pressed into rectangular green bodies at approximately 35 MPa to fabricate porous ceramics. The resulting bodies were sintered at 1200 °C for 2 h to produce a homogeneous grain size. The porosity of porous STF35 specimen was geometrically determined based on its relative density, measured to be 38%. The resulting STF35 porous specimens were used for electrical conductivity relaxation measurements to measure the oxygen exchange coefficient.

### 2.2. Fabrication of STF35 symmetric cells

STF35 symmetric cells were prepared to measure their area-specific resistance. The calcined STF35 powders were mixed with an ink vehicle (Fuelcellmaterials) in a weight ratio of 1:1 to form a slurry. STF35 ink was screen-printed onto both sides of the YSZ (100) single-crystal substrate (MTI, doubly polished,  $10 \times 10 \times 0.5 \text{ mm}^3$ ) and then dried and subsequently annealed in a tubular furnace at 1050 °C for 2 h at a heating/cooling rate of 5 °C/min. Silver paste (Fuelcellmaterials) was then applied to both sides of each of the prepared STF35 electrodes as current collectors.

### 2.3. Physical and chemical characterization

The microstructures of pristine and serially infiltrated porous STF35 bulk ceramics were examined by Zeiss Merlin High-Resolution scanning electron microscopy. Transmission electron microscopy (TEM, Talos F200X, FEI) combined with energy dispersive X-ray spectroscopy (EDX) scans were utilized to identify the microstructure of STF35 and distribution of additives. Samples for study were prepared by abrading the pristine, Cr-infiltrated, and Cr/Ca-infiltrated STF35 ceramics and dispersing the abraded material in ethanol. The local chemistry of pristine, Cr-infiltrated and Cr/Ca-infiltrated STF35 bulk ceramics was analyzed by X-ray photoelectron spectroscopy (XPS) using a Physical Electronics Versaprobe II spectrometer equipped with a monochromatized Al K-alpha X-ray source with 1486.68 eV by examining and analyzing the XPS spectra associated with O 1 s, Sr 3d, Fe 2p, Ti 2p, Cr 2p, and Ca 2p levels. Raman spectra are measured using a Renishaw Invia Reflex

Micro Raman system with wavelength of 532 nm.

### 2.4. Electrical conductivity relaxation measurements

Four gold wires were wound around the porous STF35 bulk ceramics with gold paste painted along the wires to ensure good electrical contact. Electrical conductivity relaxation measurements were performed with a HP3478A digital multimeter in a four-wire resistance measurement mode. The measurements were conducted in an alumina tube at temperatures of 275–550 °C, depending on infiltrants, with  $p\text{O}_2$  step between 0.1 and 0.2 atm, controlled by two mass-flow controllers that mixed ultrahigh purity nitrogen and oxygen (grade 5.0, Airgas). Cr and Ca nitrate-based solutions were prepared for Cr and Ca infiltrations, respectively, in ethanol to concentrations of 0.002 M (for 0.02 at%) and 0.2 M (more than 0.1 at%) for low and high loading. The pristine STF35 specimen without infiltration was first measured to extract the initial  $k_{chem}$  values to serve as reference for comparison. Following subsequent Cr-infiltration, measurements were repeated two times until the Cr concentration reached 0.3 at%. This Cr-poisoned specimen was then subsequently infiltrated with Ca-species beginning at 0.1 at% and the measurements were repeated three times until the Ca concentration reached 0.5 at%. The detailed infiltration procedures were previously described [43].

### 2.5. Electrochemical measurements of symmetric cells

The electrochemical performance of the prepared pristine, Cr-infiltrated, and Cr/Ca-infiltrated STF35 symmetric cells was investigated by electrochemical impedance spectroscopy measurements with a Solartron 1255 HF frequency response analyzer interfaced with an EG&G PAR potentiostat model 273 A with AC perturbation of 20 mV in the frequency range of 0.01 Hz to 1 MHz, and in the temperature range of 450 – 650 °C, at an oxygen partial pressure between 0.1 and 1 atm. The cells were placed inside of a continuous-flow alumina tube under gas mixtures of oxygen and nitrogen delivered through digital mass flow controllers. The obtained Nyquist plots were analyzed by using Zview software. Distribution relaxation of time (DRT) analyses were carried out with DRTtools in order to investigate the characteristic processes in more detail [54,55].

### 2.6. Electrochemical testing of anode-supported single fuel cells

The cell performances of the pristine, Cr-infiltrated, and Cr/Ca-infiltrated STF35-based single fuel cells in a configuration of Ni-YSZ/YSZ/GDC/STF35 were evaluated using a button-cell reactor. A ceramic adhesive (Ceramabond 552-VFG, Aremco) was employed to seal the cells. Humidified hydrogen (3%  $\text{H}_2\text{O}$ –97%  $\text{H}_2$ ) and air were applied as the fuel and oxidant to the anode and cathode for power output measurements, respectively. Impedance spectra were measured using a PARSTAT 4000 A Potentiostat (AMETEK Inc.) under open circuit voltage in the frequency range of 0.1 Hz–1 MHz with an AC perturbation of 15 mV. The typical current ( $I$ )-potential ( $V$ )-power density ( $P$ ) curves of the single fuel cells were recorded at operating temperatures from 650 to 500 °C at intervals of 50 °C. The stabilities of the current and power densities were recorded under a constant potential of 0.75 V at 600 °C for 110 h.

## 3. Results

### 3.1. Fabrication of infiltrated porous STF35 ceramics

In order to systematically examine the effect of surface additives on  $k_{chem}$  via conductivity relaxation measurements, there is a need to optimize the geometric morphology of porous bulk STF35 ceramics so that the overall reaction with oxygen molecules is governed solely by the surface reaction, with no contribution from the bulk diffusion of oxygen

ions. Bulk STF35 ceramics were fabricated to control both porosity and surface area by appropriate manipulation of mechanical pressure during uniaxial pressing and the subsequent sintering temperature of the porous pellets. The as-prepared STF35 powders exhibited, as desired, the cubic perovskite phase, with grains highly oriented along the (110) direction, with no evidence for secondary phases (Fig. S1, Supporting information). Higher pressures applied during pressing and higher sintering temperatures led, as expected, to lower porosity and surface area (Fig. S2, Supporting information). The porosity and surface area required optimization to ensure that reliable  $k_{chem}$  values could be obtained experimentally within desired temperature measurement windows. For example, while a highly dense bulk STF35 ceramic fabricated under high pressure and sintering temperature was found to exhibit conductivity transient profiles with multiple contributions to the overall kinetics (Fig. S3, Supporting information), the exchange kinetics of a highly porous ceramic were too fast to be measured effectively, even at reduced temperatures. Fig. 1A shows the scanning electron microscopy (SEM) images of the microstructure of an optimized pristine porous STF35 ceramic, exhibiting a geometrically determined porosity of 38% (based on lattice constant and resulting theoretical density[56]) similar to the typical cathode porosity of approximately 40% commonly used in SOFCs[13], and with a grain size of on the order of 1  $\mu\text{m}$ . This specimen was used as a reference to provide reliable  $k_{chem}$  values and to show how the presence of acidic Cr-based surface additives impede the oxygen exchange rate, and how subsequent infiltration with basic Ca-additives can compensate such initial degradation. Fig. 1B shows the microstructures of a STF35 sample successively infiltrated with Cr- and Ca-additives for a total of five consecutive measurements, confirming that the infiltration of additives had little impact on microstructural evolution.

A high-resolution transmission electron microscopy (HRTEM) image of the pristine STF35 ceramics show lattice fringes with d-spacing distance of 0.273 nm corresponding to the (110) plane of the perovskite structure (confirmed by XRD analysis), consistent with a lattice constant of 0.389 nm (Fig. S4, Supporting information), and well-matched with previously reported values [56]. Scanning transmission electron microscopy (STEM) with energy-dispersive X-ray (EDX) mapping analysis

was performed to observe the distribution of Cr- and Ca-additives on the STF35 surface. Fig. 1C-E show STEM images of the pristine, Cr-infiltrated, and Cr/Ca-infiltrated along with EDX elemental mapping. All elements in the pristine STF35 sample were evenly distributed in the lattice (Fig. 1C). The Cr-infiltrated STF35 sample also displays uniform distribution of all elements excepting for Cr (Fig. 1D). This indicates that Cr-infiltration leads to the development of various sizes of Cr-species on the STF35 surfaces, ranging from atomically distributed coverage to larger agglomerates up to  $\sim 100$  nm. This may provide insight into how the different contributions of such various Cr-regions impact the overall  $k_{chem}$  and ASR values. Fig. 1E presents the STEM-EDX images of Cr/Ca-infiltrated STF35 samples, again confirming similar distribution of the various sized Cr-regions. Ca-infiltration, however, appears to lead to the preferential distribution of Ca-species over Cr-poisoned sites, in particular along grain boundaries. This preferential reaction of the Ca and Cr species can be expected to reduce the acidic character of the Cr species as discussed below.

### 3.2. Surface characterization of infiltrated porous STF35 Ceramics

We conducted X-ray photoelectron spectroscopy (XPS) analysis of the various surfaces associated with the pristine, Cr-infiltrated, and Cr/Ca-infiltrated STF35 samples. While the XPS spectra of O 1 s, Sr 3d, and Fe 2p spectra were found to be markedly impacted by surface additives (Fig. 2A-C), Ti 2p, Cr 2p, and Ca 2p spectra remained nearly unchanged (Fig. S5, Supporting information). The O 1 s region, for all samples, was fitted with three components (Fig. 2A), consisting of two distinct main peaks at low and medium binding energies and a weak peak at a higher binding energy, that are ascribed to the bulk perovskite lattice ( $\text{O}_{\text{lattice}}$ ), adsorbed oxygen ( $\text{O}_{\text{adsorbed}}$ ), and carbonate species ( $\text{O}_{\text{carbonate}}$ ), respectively [33,57–59]. The results show that while Cr-infiltration depresses the  $\text{O}_{\text{adsorbed}}/\text{O}_{\text{lattice}}$  ratio, Ca-infiltration serves to enhance this ratio above even that of pristine STF35, indicating that adsorbed oxygen molecules are depleted on Cr-infiltrated surfaces, but prefer to adsorb on Ca-infiltrated STF35 surfaces. These observations could be related to the respective depletion and accumulation of electrons by Cr- and Ca-species, required for charge transfer from the lattice to the adsorbed

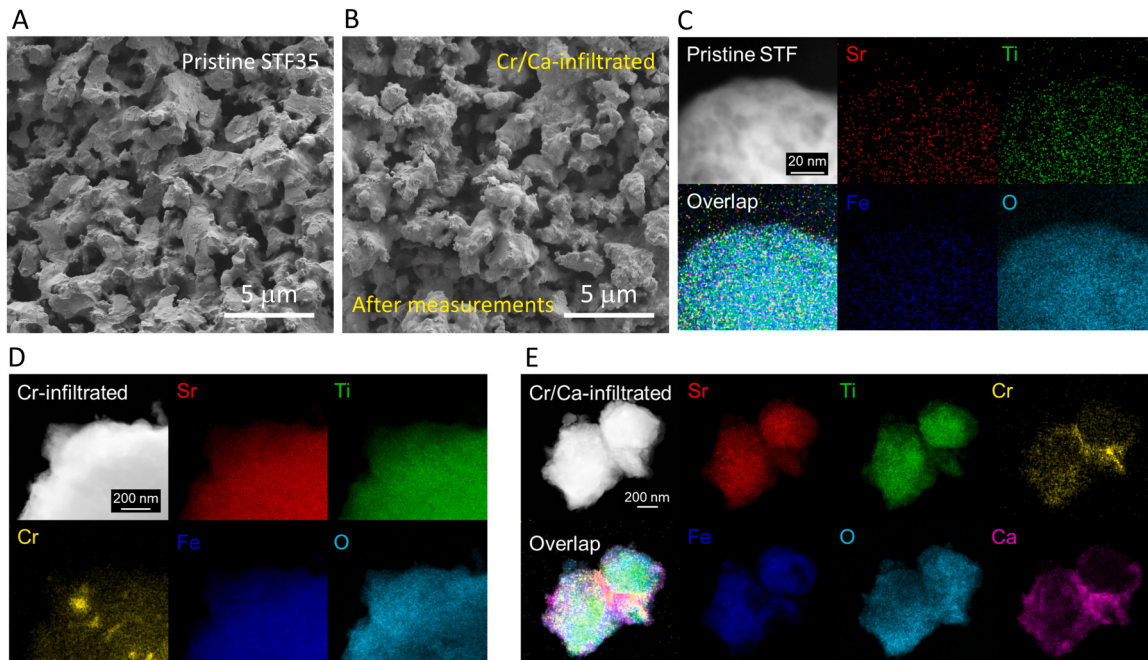


**Fig. 1.** Microstructures of the pristine, Cr-infiltrated, and Cr/Ca-infiltrated porous bulk STF35 ceramics. (A,B) Cross-sectional SEM images of (A) pristine STF35 (B) following serial infiltration with Cr(0.3 at%)/Ca(0.5 at%). (C-E) STEM images along with EDX element mapping of (C) pristine, (D) Cr-infiltrated, and (E) Cr/Ca-infiltrated STF35 bulk ceramics. All specimens analyzed following infiltration and conductivity relaxation measurements.

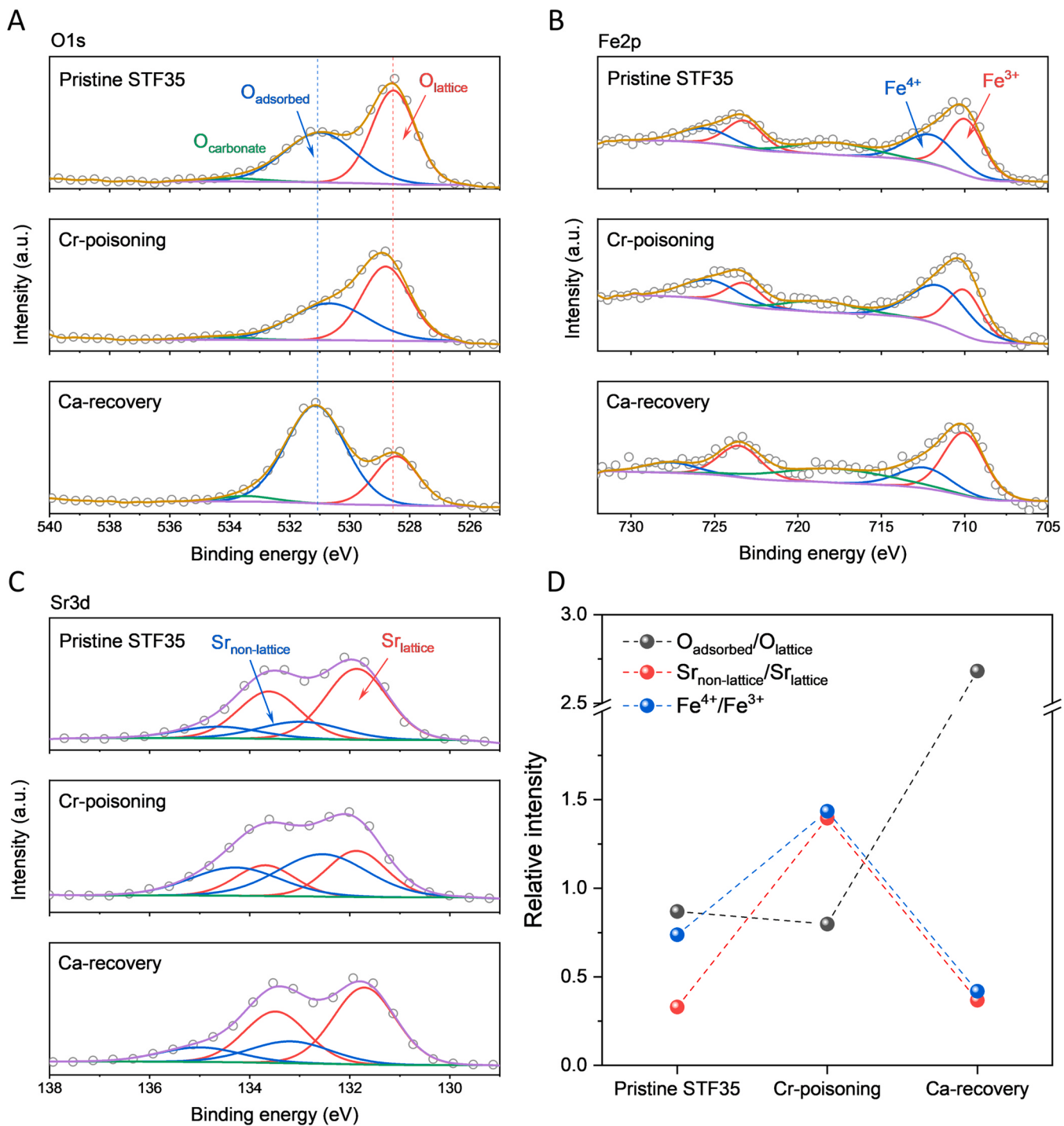


**Fig. 2.** XPS spectra of the pristine, Cr-infiltrated, and Cr/Ca-infiltrated porous STF35 bulk ceramics. (A-C) XPS spectra of (A) O 1 s, (B) Fe 2p, and (C) Sr 3d of the pristine, Cr-infiltrated, Cr/Ca-infiltrated STF35 samples. (D) Comparison of relative intensity of  $O_{\text{adsorbed}}/O_{\text{lattice}}$ ,  $\text{Sr}_{\text{non-lattice}}/\text{Sr}_{\text{lattice}}$ , and  $\text{Fe}^{4+}/\text{Fe}^{3+}$  of the pristine, Cr-infiltrated, and Cr/Ca-infiltrated STF35 samples. All specimens analyzed following infiltration and conductivity relaxation measurements.

oxygen species [57]. This expected relative change in surface electron density can be further be confirmed by noting the change in the  $\text{Fe}^{4+}/\text{Fe}^{3+}$  ratio, according to serial infiltration of Cr vs Ca-species (Fig. 2B). While Cr-infiltration leads to oxidation of Fe from 3+ to 4+, Ca-infiltration induces instead the re-reduction of Fe from 4+ to 3+. Fig. 2B shows the Sr 3d spectra of those samples, deconvoluted into two sets of spin-orbit split doublets with an area ratio of 2:3. We assign the one doublet at lower binding energy and the other at higher binding energy to Sr within the perovskite lattice ( $\text{Sr}_{\text{lattice}}$ ) and non-lattice Sr at the surface ( $\text{Sr}_{\text{non-lattice}}$ ), respectively [32,46]. While the Cr-infiltration

leads to enhanced Sr segregation (increased ratio of  $\text{Sr}_{\text{non-lattice}}/\text{Sr}_{\text{lattice}}$ ), it is significantly reversed by subsequent infiltration of Ca-species, suggesting that the surface additives influence the level of Sr surface segregation. This observation is consistent with expected elastic-driven  $\text{Sr}_{\text{non-lattice}}$  changes resulting from lattice expansion/contraction induced by changes in the oxidation state of Fe (diameter of  $\text{Fe}^{3+}$  (0.645 Å) >  $\text{Fe}^{4+}$  (0.585 Å)). We return below to this very interesting observation suggesting that Cr poisoning of the ORR may, at least in part, be much more complicated than simply referring to the Cr-rich phases formed on the cathode surface. Three distinct aspects should be

considered: i) depression of adsorbed oxygen molecules, ii) Cr-acidity-driven electron depletion leading to change in oxidation state of the B-site element (Fe in this case), and iii) enhanced Sr surface segregation induced by change in local lattice strain. On the contrary, infiltrated Ca-additives serve to neutralize the acidic nature of the Cr-impurities as well as suppress Sr segregation. XPS results on the other hand show that the ratio of  $\text{Cr}^{6+}/\text{Cr}^{3+}$  remains nearly constant regardless of Cr- and Ca-infiltrations presumably since the Cr species, being second phases, are less sensitive to charge redistributions within the STF support material (Fig. S5B, Supporting information). The relative intensity trends of the characterized ratios of  $\text{O}_{\text{adsorbed}}/\text{O}_{\text{lattice}}$ ,  $\text{Sr}_{\text{non-lattice}}/\text{Sr}_{\text{lattice}}$ , and  $\text{Fe}^{4+}/\text{Fe}^{3+}$  are summarized in Fig. 2D. Furthermore, Raman spectroscopic measurements were conducted to further understand the interaction between surface infiltrants and STF35 (Fig. S6, Supporting information). While the Cr-infiltrated STF bar shows two main characteristic peaks corresponding to  $\text{Cr}_2\text{O}_3$  ( $\text{Cr}^{3+}$ ) and chromate ( $\text{CrO}_4^{2-}$ ,  $\text{Cr}^{6+}$ ) at near  $347 \text{ cm}^{-1}$  and  $860 \text{ cm}^{-1}$  [60], respectively, consistent with previous XPS Cr 2p spectra, no significant change in the Raman spectra was observed in the Cr-infiltrated sample, meaning that not only  $\text{Cr}_2\text{O}_3$  but also additional compound phase of  $\text{SrCrO}_4$  should co-exist upon Cr-infiltration. Meanwhile, infiltrated Ca can also react with the Cr-species forming  $\text{CaCrO}_4$ , but it is difficult to distinguish between  $\text{CaCrO}_4$  and  $\text{SrCrO}_4$  by Raman spectroscopy. While the formation energy of  $\text{SrCrO}_4$  phase is lower than that of  $\text{CaCrO}_4$  [61], nevertheless, we found by XPS that the non-lattice Sr peak which would be associated with  $\text{SrCrO}_4$  decreased upon the addition of the Ca-species, suggesting therefore that  $\text{CaCrO}_4$  is the likely product formed. Again, it should be noted that surface acidity engineering can play an important role in tuning surface activity as well as surface cation segregation by modulating surface electron density and resulting change in lattice constant at the surface. Taken together, those trends are in line with our hypothesis that acidic Cr-species tend to depress the electron density and adsorbed oxygen, while increasing segregated Sr, while subsequent serial infiltration of basic Ca-species serve to replenish the depleted electrons and adsorbed oxygen while depressing the segregated Sr species at the STF35 surface respectively, which has not been previously reported, to best of our knowledge.

### 3.3. Oxygen exchange coefficients of infiltrated bulk STF35 ceramics

As the oxygen stoichiometry of STF35, and thereby its electrical conductivity changes with oxygen partial pressure under oxidizing conditions, it is possible to determine the kinetics associated with the uptake or release of oxygen by monitoring the conductivity transient upon a step change in oxygen partial pressure [62]. There are several factors that contribute to the overall exchange kinetics, including oxygen diffusion within the oxide solid, characterized by  $D_O$ , and rate of oxygen exchange between the solid and the gas phase characterized by  $k_{\text{chem}}$ , and gas phase diffusion within the pores [63,64]. In order to isolate the  $k_{\text{chem}}$  contribution to the overall kinetics, one needs to select geometries in which the kinetics are limited only by the surface exchange reaction, achieved when the physical diffusion length within the solid is shorter than the so-called critical thickness, defined by  $L_c \leq \frac{D}{k}$  [65]. This can be satisfied, for example, by selecting a dense film with thickness [66], or grain size in a porous ceramic (as in this study)  $< L_c$ , respectively. Here we fabricated highly porous STF35 bulk ceramics, as in our preceding studies on porous PCO ceramics [43,44], with grain sizes less than  $1 \mu\text{m}$ , more than 2 orders of magnitude lower than the critical thickness (approximately  $200 \mu\text{m}$  at  $700^\circ\text{C}$  [67]) in STF35. The pristine specimen was first measured and then infiltrated with the Cr-species at a dilute concentration of 0.02 at% with respect to STF35 and re-measured. The process was repeated to incrementally monitor the  $k_{\text{chem}}$  dependence on the loading level of Cr-infiltration (up to 0.3 at%), then followed by successive infiltration of Ca-species ranging from 0.1 to 0.5 at%.

Fig. 3A shows the normalized conductivity relaxation profiles of pristine STF35 at  $400^\circ\text{C}$  following a step change in oxygen partial pressure from 0.1 to 0.2 atm, and after a series of subsequent Cr- and Ca-infiltrations.  $k_{\text{chem}}$  values were calculated with the aid of the first order reaction for the conductivity transient, with the detailed information in Supplementary Note 1, Fig. S7, and Table S1 in Supporting information [43].  $k_{\text{chem}}$  was found to significantly decrease with increasing Cr-additive levels, ultimately leading to a depression in  $k_{\text{chem}}$  by over two orders of magnitude. Successive infiltration of Ca-species, beginning with 0.1 at%, led to increasing levels of recovery of the Cr-poisoned exchange rate, ultimately returning to nearly that of the pristine value, as shown in Fig. 3B. Arrhenius plots of the  $k_{\text{chem}}$  values determined for the pristine STF35 specimen, and for following subsequent Cr- and Cr/Ca-infiltrated conditions, are presented in Fig. 3C. While the measured  $k_{\text{chem}}$  values strongly depend on the level of infiltration, the obtained  $E_a$  values, centered at approximately 1.4 eV, are consistent with the literature on  $\text{SrTi}_{0.7}\text{Fe}_{0.3}\text{O}_{3-\delta}$  (STF30) [68], and show little dependence on infiltration (Fig. S8 and Table S2, Supporting information). These findings are in line with our previous work on fluorite-based MIEC PCO ceramics [43,44].

### 3.4. Electrochemical evaluation of infiltrated STF35 symmetric cells

Electrochemical impedance spectroscopy (EIS) was applied to verify the findings of the conductivity relaxation measurements, in which infiltration with Cr-species decreased the oxygen exchange reaction rate, while basic Ca-species additives acted to compensate the degradation. This offers the opportunity to examine if measured changes in reaction rate correlate well with corresponding changes in electrochemical polarization resistance. Symmetrical cells were prepared with two nominally identical STF35 electrodes with thickness of  $\sim 16 \mu\text{m}$ , screen-printed onto both sides of an YSZ single-crystal substrate (Fig. S9, Supporting information). Fig. 4A presents a typical impedance spectrum, plotted in Nyquist form, consisting of several overlapping semi-circles. Note that the resulting overall electrode resistance ( $R_{\text{electrode}}$ ) of the pristine symmetric cell falls within reported values ( $\sim 0.7\text{--}6.0 \Omega\cdot\text{cm}^2$ ) [13,52] with STF with more than 70% iron expected to offer higher performance than that of STF with low iron content. The dramatic increase in  $R_{\text{electrode}}$  by nearly an order of magnitude was observed in the 2 at% Cr-infiltrated cell, in agreement with similar trends observed for  $k_{\text{chem}}$  values. Upon serial infiltration of the Cr-poisoned cell by 2 at% Ca-additives,  $R_{\text{electrode}}$  showed a seven-fold decrease, nearly returning it to that of the initial pristine STF35 cell while maintaining activation energies of  $\sim 1.2 \text{ eV}$  (Fig. 4B). Furthermore, the pristine and infiltrated STF35 cells retained the dependence of  $R_{\text{electrode}}$  on  $p\text{O}_2^{\text{m}}$  with  $m \sim 0.2\text{--}0.3$  slope, similar to the reported value of 0.25 for STF electrodes, reflective of the surface reaction controlled process (Fig. S10, Supporting information) [20]. In order to be able to more effectively deconvolute contributions from various processes to the overall impedance spectra in the Nyquist plots, the distribution of relaxation time (DRT) analysis was performed [55,69]. Characteristic DRT plots obtained at  $600^\circ\text{C}$  with  $p\text{O}_2$  of 0.2 atm for the pristine STF35 symmetric cell, and with subsequent serial infiltration of Cr- and Ca-species, are illustrated in Fig. 4C. Several weaker peaks with short time constants below  $10^{-3} \text{ sec}$  show little or no influence of infiltration and are assumed to be related to oxygen transfer across the electrode-electrolyte interface [70]. Three considerably larger peaks are observed in the Cr-infiltrated samples, P1, P2, and P3 (see Fig. 4B) at longer time constants, with P1 also clearly apparent for the pristine and Ca/Cr-infiltrated conditions. One finds that the spectra associated with dilute Cr-infiltration (0.36 at%) exhibits the additional P2 peak, followed by the appearance of the P3 peak at high Cr-concentration (2 at%) (Fig. S11A and B, Supporting information). Arrhenius plots of these DRT peaks and  $p\text{O}_2$  dependence of  $R_{\text{electrode}}$  showed nearly equal  $E_a$  and  $m$  values, respectively, regardless of Cr-infiltration levels (Fig. S11C and D, Supporting information). Note that gas diffusion contributions within

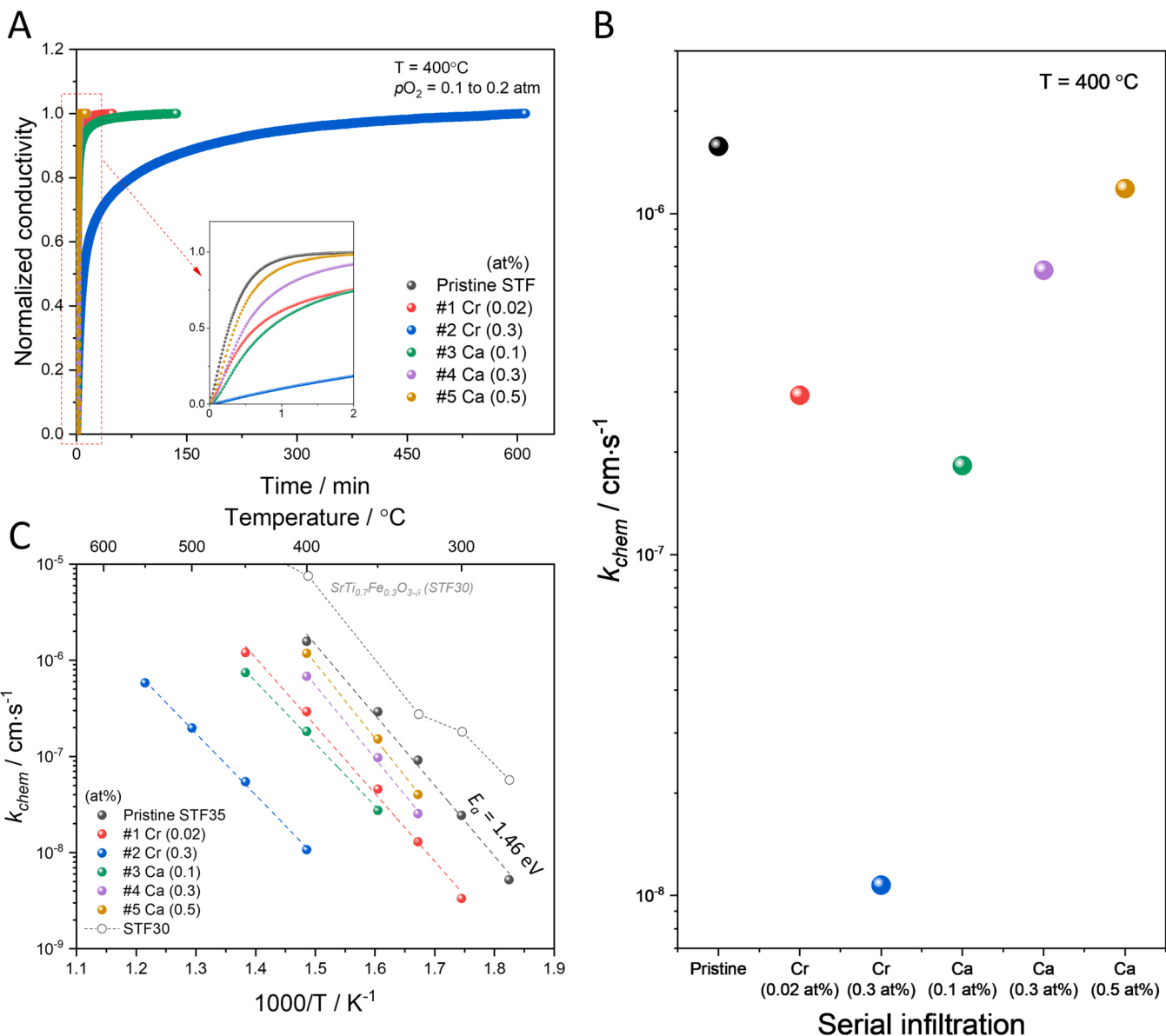


**Fig. 3.** The oxygen exchange kinetics of pristine, Cr-infiltrated, and Cr/Ca-infiltrated porous bulk STF35 ceramics, (A) Normalized conductivity relaxation profiles measured at 400°C in response to a  $p\text{O}_2$  step (0.1–0.2 atm) beginning with a pristine bulk STF35 ceramic and following successive Cr- and Cr/Ca-infiltrations. (B) Log  $k_{\text{chem}}$  for STF35 evaluated at 400°C vs the serial infiltration levels of Cr followed by Ca-infiltration. (C) Arrhenius plots of  $\log k_{\text{chem}}$  vs reciprocal temperature for the pristine, Cr- and Cr/Ca-infiltrated STF samples. Dashed lines reflect the best fits to the data. Earlier published STF30 data by Merkle et al. are included for comparison[68].

the pores, typically observed at lower frequency regimes, can be readily eliminated in this work given the predicted weak temperature-dependent characteristic of this process. Based on these observations, one can infer that several distinctly different types of active surface regions exist, characterized by different rates of oxygen exchange induced by Cr-species, as previously observed in the distribution of Cr-species by STEM-EDX mapping (Fig. 1D). In other words, the peaks corresponding to P1, P2, and P3 suggest the existence of distinctive zones characterized by regions for which Cr spatial distribution varies from atomic, to nanocluster, and to larger agglomerates [71]. Serial infiltration of Ca-infiltration resulted in a reversal of the poisoned characteristic peaks, ultimately recovering their electrochemical performance. Note that the ability of basic Ca-additives, on their own, to boost the initial ORR activity of the STF35 electrode was confirmed, by showing a two-fold performance enhancement while maintaining the same temperature and  $p\text{O}_2$  dependence (Fig. S12,

*Supporting information*). These findings support the contention that controlled surface acidity aids in recycling or recovering poisoned fuel cell electrodes.

### 3.5. Demonstration of single fuel cell performance with controlled acidity

While measurements of the impact of acidic/basic additives on oxygen exchange kinetics, and on the polarization resistance of symmetric cells, are clear indicators of their role in impacting the ORR kinetics of SOFC cathodes, it is instructive to demonstrate their impact directly on SOFC power outputs. Therefore, to demonstrate the feasibility of the use of controlled acidity as a tool for reversing the performance of degraded fuel cell devices, typical anode-supported Ni-YSZ/YSZ/GDC/STF35 single cells (Fig. S13, *Supporting information*), both prior to, and following infiltration of 2 at% Cr- and 4 at% Ca-species, were utilized to evaluate their fuel cell performance. Note that a higher concentration of

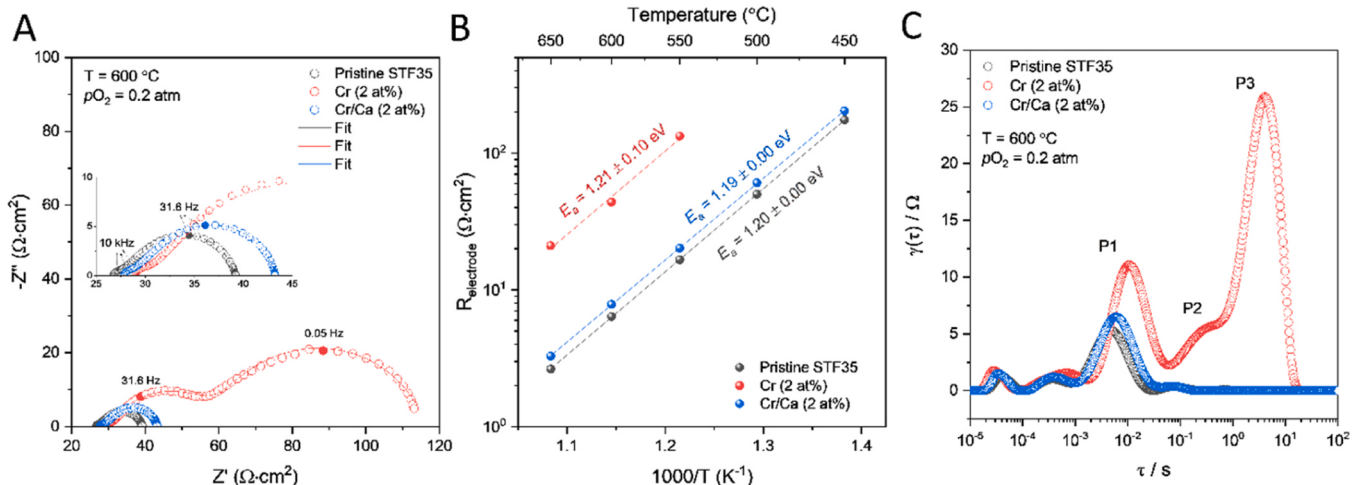


**Fig. 4.** EIS results of pristine, Cr-infiltrated, and Cr/Ca-infiltrated STF35 symmetric cells. (A) Complex impedance plots of pristine, Cr-infiltrated, and Cr/Ca-infiltrated STF35 electrodes measured at 600 °C with  $pO_2 = 0.2$  atm. (B) Arrhenius plots of electrode resistance ( $R_{\text{electrode}}$ ) vs reciprocal temperature of pristine, Cr-infiltrated, and Cr/Ca-infiltrated STF35 electrodes. (C) DRT plots derived from corresponding Nyquist plots in part A.

infiltrated Ca-species was selected relative to that of the infiltrated Cr-species. This followed from our previous observations of our conductivity relaxation and symmetric cell tests that a comparable amount of Ca to Cr infiltration only returned the degraded performance back to that of the pristine device. On the other hand, an excess of Ca relative to the Cr content appeared necessary to achieve conditions in which the Ca/Cr co-infiltrated cell would outperform the initial pristine device activity, with the excess Ca expected to further reduce any remaining detrimental effects derived from Sr segregation and Cr-specie poisoning. Fig. 5A shows current ( $I$ )-voltage ( $V$ ) and power density ( $P$ )  $I$ - $V$ - $P$  curves of single cells recorded at 650°C under humidified H<sub>2</sub> (3% H<sub>2</sub>O-97% H<sub>2</sub>) as the fuel and dry air as the oxidant. The resulting peak power densities of the pristine, Cr-infiltrated, Cr/Ca-infiltrated single fuel cells reach 170, 105, and 190 mW·cm $^{-2}$ , respectively. The reader should keep in mind that the scope of this work was not to showcase word-record fuel cell performance, but to demonstrate the reversal of Cr-driven performance degradation by subsequent surface modification of electrodes with infiltrants with controlled acidity. Approximately a 40% reduction in cell performance upon Cr-infiltration should be considered severe given that acceptable Cr-induced degradation rates of cells are reportedly 0.2–0.5% per 1000 h [72]. Remarkably, the Ca-recovery step led to a dramatic 80% recovery in peak power density, thereby outperforming

the power output of the pristine cell. The origins of its depression and recovery were examined by studying the polarization losses of the overall cell by impedance spectroscopy, as plotted in Fig. 5B. While the offset resistance associated with the ohmic loss is weakly dependent on infiltration, the polarization resistance resulting from the cathode shows a strong dependence on infiltration, as presented in Fig. 5C. Note that since STF-based fuel cells were already demonstrated by Zhang et al. to be capable of offering performance comparable to or better than commercial LSCF-based cells [13], their fuel cell performance can be expected to be further improved by application of the demonstrated acidity/basicity infiltration strategy. In short, to the best of our knowledge, this work demonstrates, for the first time, the capability of engineering surface acidity/basicity to reverse chronic fuel cell degradation, resulting from the combination of intrinsic Sr segregation and extrinsic Cr-poisoning occurring on Co-free perovskite-based cathodes. While similar concepts were previously demonstrated by our group for the model MIEC fluorite-structured PCO material, that simpler binary structure did not suffer, as well, from the issues related to Sr (or Ba) A-site segregation, characteristic of the perovskite structure. [43,73].

To demonstrate the stability of the Ca-refreshed cell following Cr-poisoning, the current density and corresponding power densities of the refreshed fuel cell were evaluated at 600°C under a constant voltage

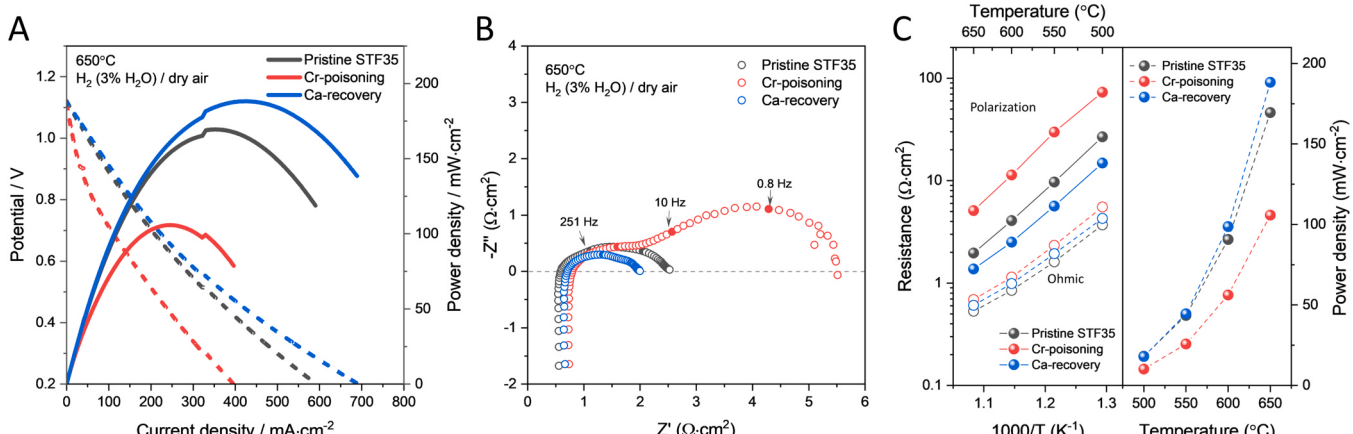


**Fig. 5.** Electrochemical performance of the pristine, Cr-infiltrated, and Cr/Ca-infiltrated STF35 single fuel cells. (A) I-V-P curves and (B) impedance spectra of the pristine, Cr-infiltrated, and Cr/Ca-infiltrated STF35 single fuel cells measured at 650°C under wet H<sub>2</sub> at the anode and air at the cathode. 2 at% Cr and 4 at% Ca infiltrations were used for poisoning and recovery sources, respectively. Note that  $I$  denotes current density,  $V$  potential, and  $P$  power density. (C) Comparison of resulting ohmic and polarization resistances, and peak power densities of the cells at  $T = 500 - 650$  °C.

of 0.75 V for 110 h, as presented in Fig. 6A. No noticeable performance degradation was observed, but rather the performance was found to improve, as indicated by an increase in current density with time during the 110 h of operation. Fig. 6B demonstrates a further increase in peak power density by 42% after 110 h of operation, compared to the initial performance of the Ca-recovered electrode. Indeed, these Ca-recovered results represent a nearly 160 % improvement over the Cr-poisoned results. These improvements resulted not from ohmic resistance but rather cathode polarization resistance changes, as plotted in Fig. 6C. These improvements with time can be reasonably attributed to the excess Ca-infiltration (4 at%) relative to Cr (2 at%), potentially affecting i) further depression in concentration of segregated Sr rich regions, and ii) increased surface electron density, as previously observed by examination of the  $\text{Sr}_{\text{non-lattice}}/\text{Sr}_{\text{lattice}}$  and  $\text{Fe}^{4+}/\text{Fe}^{3+}$  ratios in the XPS analysis (Fig. 2D). The observed increase in current density with time in Fig. 6A would be consistent with excess Ca infiltrants progressively scavenging the Cr-based residues over time. One may also wish to consider the potential decomposition of any  $\text{CaCO}_3$  initially formed into  $\text{CaO}$  and  $\text{CO}_2$  at these elevated temperatures [74], thereby reducing the more acidic character of  $\text{CaCO}_3$  compared to that of  $\text{CaO}$ . Nevertheless, further studies are required to confirm the source of the observed performance improvement with time.

#### 4. Discussion

Several elemental processes have been suggested as the rate-determining step (RDS) in the ORR on perovskite-based electrodes, including i) adsorption of oxygen molecules, ii) their dissociation, iii) charge transfer of electrons to the adsorbed oxygen species, and iv) incorporation of oxygen ions into the oxygen vacancies within the lattice. In an earlier study, based on the magnitude of the measured activation energies of  $R_{\text{electrode}}$  as a function of Fe content, and the characteristic 0.25 slope dependence of  $\log R_{\text{electrode}}$  on  $\log p_{\text{O}_2}$  for STF35 electrode, the electron transfer process was viewed as the RDS for ORR on the STF surface in the high  $p_{\text{O}_2}$  regime [20]. In this study, we were able to vary the electron density at the STF surface, by orders of magnitude, by controlling the relative acidity/basicity of binary oxides infiltrated on the STF35 surface, while keeping the Fe content fixed, viz. STF35. As observed in our earlier studies on PCO [42–44], acidity and basicity induced changes in  $R_{\text{electrode}}$  are largely reflected in changes in the pre-exponential factor ( $A$ ), and not in  $E_a$  or the  $p_{\text{O}_2}$  dependence (Fig. 4B and Fig. S8), respectively, implying that the surface additives used in this work do not act as electro-catalysts directly influencing the activation energy, but rather impact the concentration of electrons required for the charge transfer reaction. Thus, introducing acidic

chromia leads to depletion of electrons, while basic calcia replenishes the surface electron density, ultimately reversing the initial degraded performance induced by chromia infiltration. These observations are consistent with our previous study in which the effects of individual binary oxides on  $k_{\text{chem}}$  on PCO were studied [42] and with the De Souza model [75], in which the pre-exponential factor  $A$ , is proportional to the surface electron concentration, that we view as responsible for the marked changes observed in  $k_{\text{chem}}$ ,  $R_{\text{electrode}}$ , and SOFC power output of STF35-based structures and cells, depending on the surface infiltrants utilized.

Because surface infiltrants are not expected to be incorporated into the STF35 lattice to any significant degree given the relatively low operating temperatures of this study (< 650°C), they are therefore expected to have only a very marginal effect on its electrical conductivity, as confirmed in Fig. S14 in Supporting information. Here one observes only a very weak dependence of conductivity on infiltration ranging from a few to tens of percentage points without change in activation energy. A very marginal effect, when compared to the variation in  $k_{\text{chem}}$  by more than 10,000 %. Furthermore, given the various changes observed in this work related to Sr segregation and Fe valence state in the vicinity of the surface, it becomes very challenging to understand and define the main source of the observed conductivity changes. In contrast to our previous works on Pr-doped  $\text{CeO}_2$  that was free of Sr segregation, the situation here is more complex. Indeed, one expects that the effects of Sr segregation, on the one hand and Fe valence state change on the other, would be expected to have opposite effects on the p-type conductivity of STF. For example, acidic Cr additives serve to deplete electrons or correspondingly increase holes in vicinity of the surface. Indeed, we report an increase in  $\text{Fe}^{4+}$  concentration at the surface upon infiltration with Cr and since  $\text{Fe}^{4+}$  is considered a hole due to empty states in  $\text{Fe}^{3+}/\text{Fe}^{4+}$  redox state above the top of the valence band as described by Rothschild et al., this should lead to increasing conductivity [48]. On the other hand, Cr infiltration has been shown to lead to increased Sr segregation to the surface, i.e., enriched in  $\text{SrO}$  and therefore depleted in transition metal ions, including the total Fe concentration, leading to an expected decrease in near surface hole conductivity. Since those two opposing expectations are indeed observed in our STF system with the acid/base engineering, i.e. increased  $\text{Fe}^{4+}/\text{Fe}^{3+}$  ratio and increased Sr segregation, it becomes difficult to draw conclusions at this stage in isolating the impact of the acid/base approach on the conductivity of perovskite oxides, and thus further investigation is needed.

The authors had previously demonstrated the feasibility of surface acidity engineering as an effective tool for reactivating degraded cathode reactivity on the alternative fluorite-based model PCO material free

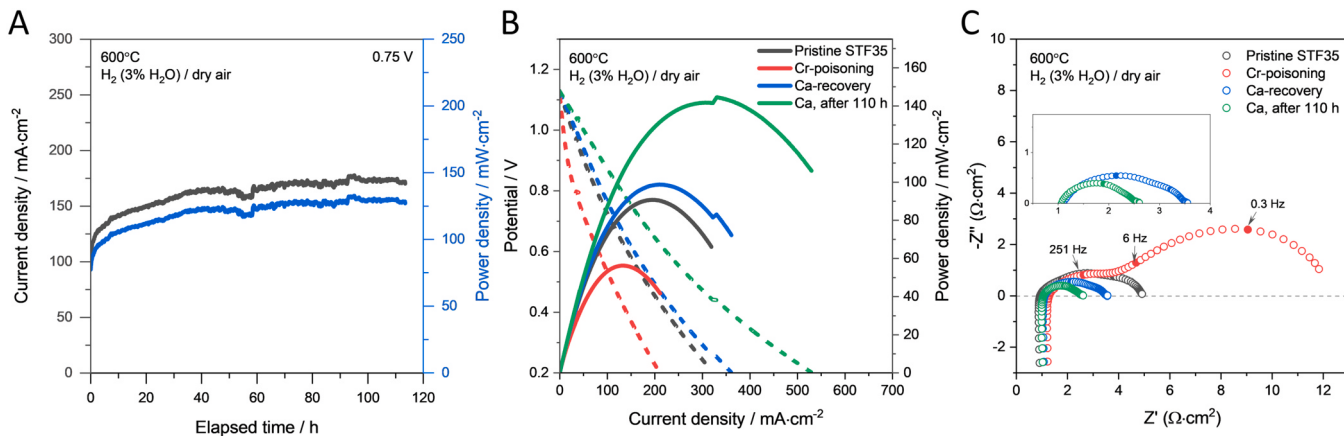


**Fig. 6.** Stability test of the Cr/Ca-infiltrated STF35 single fuel cell. (A) Long-term stability test: Current density of Cr/Ca-infiltrated STF35 single cell performed for 110 h at 600°C under a constant voltage of 0.75 V. Comparison of resulting (B) I-V-P curves and (C) impedance spectra for designated cells prior to and after long-term testing.

of Sr [43,44,73]. This succeeded in isolating the cause of such degradation induced by extrinsic acidic impurities (Cr, Si) to surface electron depletion by being able to exclude the impact of intrinsic Sr segregation on performance normally associated with the use of perovskite-based cathodes. With this work on STF, we succeeded in generalizing this strategy by demonstrating that it applies as well to the popular perovskite-structured electrode materials. These primarily Sr and transition metal element-based oxides exhibit susceptibility to two major degradation sources: i) intrinsic surface Sr segregation and ii) extrinsic acidic impurities. Given that extensive efforts to date have been invested in enhancing the initial performance of those electrodes, it was important to demonstrate that one could as well examine how surface acidity engineering can simultaneously address both issues. We were also able to address the apparently conflicting findings that Sr segregation to the surface of perovskites, on the one hand, generally leads to degradation in both oxygen exchange kinetics and cathode polarization, while more limited studies, on the other hand, suggest that excess  $\text{SrO}_x$  or other alkaline earth oxides added to such perovskite surfaces can lead to enhanced performance [35–39]. In this work, we clearly demonstrate that physical blocking of active sites by extrinsic impurities (e.g. Cr in this work) alone is not responsible for degradation, given the limited amount of Cr-loading, and contrary to conventional wisdom in MIEC perovskite cathode materials, excess alkaline earth oxides on their surfaces, e.g.  $\text{SrO}$  or  $\text{CaO}$ , do not necessarily lead to depressed performance. Indeed, it appears that the source of these alkaline earth excesses on the surface is key to their impact. Specifically, excess e.g.  $\text{SrO}_x$  segregation from within the lattice, has an opposite effect to that of the addition of a second phase, e.g., by infiltration from without. The key distinction appears to be that as a second phase, particularly the basic additives, given their lower work functions, lead to electron accumulation on the electrode surface, while enriched  $\text{SrO}_x$  on the surface serves to deplete adsorbed oxygen as per our XPS studies. A particularly interesting observation from these studies on the STF system, not previously reported, is that the subsequent infiltration of Ca following Cr-infiltration not only compensates for the acidity of the Cr-species, but also simultaneously leads to the reduction in the concentration of  $\text{Sr}_{\text{non-lattice}}$  surface relative to  $\text{Sr}_{\text{lattice}}$  species, apparently via the reduction of  $\text{Fe}^{4+}$  to  $\text{Fe}^{3+}$ . Given that this can also be extended to other state-of-the-art perovskite oxides containing transition metal cations, one expects likewise the possibility of coupling acidity/basicity induced surface electron depletion/accumulation to lead as well to transition metal oxidation/reduction, respectively. In addition, considering that Cr degradation is a continuous process during practical operating conditions, one can expect that pre-coating with a basic additive such as  $\text{CaO}$  could be used to delay the onset and ultimately limit Cr-induced degradation. Preliminary work in our laboratories indeed confirms this expectation, with our results being prepared for subsequent publication. Acid/Base engineering of surface infiltrants can therefore be expected to improve the performance of SOFC devices as well as considerably extend their operating lifetimes.

## 5. Conclusions

In this study, a surface acidity engineering strategy was proposed as an efficient route for refreshing degraded fuel cell performance, leading to enhanced long-term electrode durability. As a practical demonstration of this idea, we examined the impact of acidic Cr and basic Ca additives on three different metrics: i) oxygen exchange coefficient ( $k_{\text{chem}}$ ), ii) area-specific resistance (ASR), and iii) peak power density, by utilizing porous STF35 bulk ceramics, symmetric electrochemical cells, and anode-supported single fuel cells, respectively, the latter two utilizing screen printed porous STF35 thick films. Acidic Cr-infiltration resulted in a pronounced depression in  $k_{\text{chem}}$ , an increase in ASR, and a depression in peak power density by approximately 100, 10, and 40%, respectively. The full recovery in those metrics was achieved by adding basic Ca-species onto Cr-poisoned STF35 surfaces without significant

change in activation energy of  $k_{\text{chem}}$  or ASR. These reversals in surface degradation were attributed to the simultaneous depression in both intrinsic Sr segregation and extrinsic acidic nature of Cr-species by accumulating surface electrons while simultaneously driving the reduction of  $\text{Fe}^{4+}$  to  $\text{Fe}^{3+}$ , as revealed by XPS results. A further increase in peak power density by 42% after 110 h of operation was demonstrated compared to the initial performance of the Ca-recovered electrode, ultimately representing a nearly 160% improvement over the Cr-poisoned power output. In summary, the demonstrated ability to revive the degraded performance of MIEC perovskite electrodes has important implications not only in accelerating the commercial feasibility of SOFCs/SOECs, but in penetrating the energy market given the potential to extend the lifetime of installed systems and revive them instead of requiring their complete replacement. Beyond being impactful regarding device development central to energy conversion and storage, the proposed straightforward strategy of tuning surface acidity by varying the ratio of infiltrants based on the materials acidity scale can be also expanded to other energy technologies where the metal oxide/gas interface plays a central role, for example metal oxide gas sensors, photoelectrochemical cells, oxygen permeation membranes, solar thermochemical reaction, and oxygen storage materials in auto emissions systems.

## CRediT authorship contribution statement

**Han Gil Seo:** Writing – review & editing, Writing – original draft, Methodology, Investigation, Formal analysis, Conceptualization. **Hyunseung Kim:** Writing – review & editing, Investigation, Formal analysis. **WooChul Jung:** Writing – review & editing, Resources. **Harry L. Tuller:** Writing – review & editing, Supervision, Resources, Conceptualization.

## Declaration of Competing Interest

The authors declare that they have no known competing financial interests or personal relationships that could have appeared to influence the work reported in this paper.

## Data Availability

Data will be made available on request.

## Acknowledgements

This research was supported with funds provided by the MIT Department of Materials Science and Engineering via the R.P. Simmons Professor of Ceramics and Electronic Materials Chair. We acknowledge the use of SEM and XPS in the MIT Materials Research Laboratory Shared Experimental Facility. We particularly thank Dr. Thomas Deferriere for assistance with the Raman spectroscopy measurements. H.K. and W.J. acknowledge support from the National Research Foundation of Korea (NRF-2022K1A4A8A01080242) and by the Nano & Material Technology Development Program through the National Research Foundation of Korea (NRF) funded by Ministry of Science and ICT (RS-2024-00436418).

## Appendix A. Supporting information

Supplementary data associated with this article can be found in the online version at [doi:10.1016/j.apcatb.2024.124172](https://doi.org/10.1016/j.apcatb.2024.124172).

## References

- [1] Y. Zhang, B. Chen, D. Guan, M. Xu, R. Ran, M. Ni, W. Zhou, R. O'Hare, Z. Shao, Thermal-expansion offset for high-performance fuel cell cathodes, *Nature* 591 (2021) 246–251, <https://doi.org/10.1038/s41586-021-03264-1>.

- [2] M.A. Laguna-Bercero, Recent advances in high temperature electrolysis using solid oxide fuel cells: a review, *J. Power Sources* 203 (2012) 4–16, <https://doi.org/10.1016/j.jpowsour.2011.12.019>.
- [3] Z. Shao, W. Yang, Y. Cong, H. Dong, J. Tong, G. Xiong, Investigation of the permeation behavior and stability of a  $\text{Ba}_{0.5}\text{Sr}_{0.5}\text{Co}_{0.2}\text{Fe}_{0.2}\text{O}_{3-\delta}$  oxygen membrane, *J. Membr. Sci.* 172 (2000) 177–188, [https://doi.org/10.1016/S0376-7388\(00\)00337-9](https://doi.org/10.1016/S0376-7388(00)00337-9).
- [4] G. Dimitrakopoulos, B. Koo, B. Yildiz, A.F. Ghoniem, Highly durable C2 hydrocarbon production via the oxidative coupling of methane using a  $\text{BaFe}_{0.9}\text{Zr}_{0.1}\text{O}_{3-\delta}$  mixed ionic and electronic conducting membrane and  $\text{La}_2\text{O}_3$  catalyst, *ACS Catal.* 11 (2021) 3638–3661, <https://doi.org/10.1021/acscatal.0c04888>.
- [5] A. Steinfeld, Solar thermochemical production of hydrogen - a review, *Sol. Energy* 78 (2005) 603–615, <https://doi.org/10.1016/j.solener.2003.12.012>.
- [6] W.C. Chueh, C. Falter, M. Abbott, D. Scipio, P. Furler, S.M. Haile, A. Steinfeld, High-flux solar-driven thermochemical dissociation of  $\text{CO}_2$  and  $\text{H}_2\text{O}$  using nonstoichiometric ceria, *Science* 330 (80) (2010) 1797–1801, <https://doi.org/10.1126/science.1197834>.
- [7] T. Montini, M. Melchionna, M. Monai, P. Fornasiero, Fundamentals and catalytic applications of  $\text{CeO}_2$ -based materials, *Chem. Rev.* 116 (2016) 5987–6041, <https://doi.org/10.1021/acs.chemrev.5b00603>.
- [8] A.F. Staerz, H.G. Seo, T. Defferrriere, H.L. Tuller, Silica: ubiquitous poison of metal oxide interfaces, *J. Mater. Chem. A* 10 (2022) 2618–2636, <https://doi.org/10.1039/DITA08469K>.
- [9] K. Izawa, H. Ulmer, A. Staerz, U. Weimar, N. Barsan, Application of SMOX-based sensors, in: N. Barsan, K. Schierbaum (Eds.), *Gas Sensors Based Conduct. Met. Oxides Basics Understanding, Technol. Applications*, Elsevier, 2018, pp. 217–251.
- [10] H.G. Seo, Y. Choi, W.C. Jung, Exceptionally enhanced electrode activity of (Pr,Ce)  $\text{O}_{2-\delta}$ -based cathodes for thin-film solid oxide fuel cells, *Adv. Energy Mater.* 8 (2018) 1–7, <https://doi.org/10.1002/aenm.201703647>.
- [11] Z. Shao, S.M. Halle, A high-performance cathode for the next generation of solid-oxide fuel cells, *Nature* 431 (2004) 170–173, <https://doi.org/10.1038/nature02863>.
- [12] T. Hibino, A. Hashimoto, T. Inoue, J. Tokuno, S. Yoshida, M. Sano, A low-operating-temperature solid oxide fuel cell in hydrocarbon-air mixtures, *Science* 288 (80) (2000) 2031–2033, <https://doi.org/10.1126/science.288.5473.2031>.
- [13] S.-L. Zhang, H. Wang, M.Y. Lu, A.-P. Zhang, L.V. Mogni, Q. Liu, C.-X. Li, C.-J. Li, S. A. Barnett, Cobalt-substituted  $\text{SrTi}_{0.8}\text{Fe}_{0.7}\text{O}_{3-\delta}$ : a stable high-performance oxygen electrode material for intermediate-temperature solid oxide electrochemical cells, *Energy Environ. Sci.* 11 (2018) 1870–1879, <https://doi.org/10.1039/C8EE00449H>.
- [14] S.-N. Lee, A. Atkinson, J.A. Kilner, Effect of chromium on  $\text{La}_{0.6}\text{Sr}_{0.4}\text{Co}_{0.2}\text{Fe}_{0.8}\text{O}_{3-\delta}$  solid oxide fuel cell cathodes, *J. Electrochem. Soc.* 160 (2013) F629–F635, <https://doi.org/10.1149/2.099306jes>.
- [15] S.P. Jiang, X. Chen, Chromium deposition and poisoning of cathodes of solid oxide fuel cells - a review, *Int. J. Hydrom. Energy* 39 (2014) 505–531, <https://doi.org/10.1016/j.ijhydene.2013.10.042>.
- [16] M. Perz, E. Bucher, C. Gspan, J. Waldbäusl, F. Hofer, W. Sitte, Long-term degradation of  $\text{La}_{0.6}\text{Sr}_{0.4}\text{Co}_{0.2}\text{Fe}_{0.8}\text{O}_{3-\delta}$  IT-SOFC cathodes due to silicon poisoning, *Solid State Ion.* 288 (2016) 22–27, <https://doi.org/10.1016/j.ssi.2016.01.005>.
- [17] N. Tsvetkov, Q. Lu, L. Sun, E.J. Crumlin, B. Yildiz, Improved chemical and electrochemical stability of perovskite oxides with less reducible cations at the surface, *Nat. Mater.* 15 (2016) 1010–1016, <https://doi.org/10.1038/nmat4659>.
- [18] S.U. Rehman, M.H. Hassan, H.-S. Kim, R.-H. Song, T.-H. Lim, J.-E. Hong, D.-W. Joh, S.-J. Park, J.-W. Lee, S.-B. Lee, Designing the nano-scale architecture of the air electrode for high-performance and robust reversible solid oxide cells, *Appl. Catal. B Environ.* 333 (2023) 122784, <https://doi.org/10.1016/j.apcatb.2023.122784>.
- [19] S. Jeon, J. Seo, J.W. Shin, S. Lee, H.G. Seo, S. Lee, N. Tsvetkov, J. Kim, J. An, W. Jung, Metal-oxide nanocomposite catalyst simultaneously boosts the oxygen reduction reactivity and chemical stability of solid oxide fuel cell cathode, *Chem. Eng. J.* 455 (2023) 140611, <https://doi.org/10.1016/j.cej.2022.140611>.
- [20] W. Jung, H.L. Tuller, A new model describing solid oxide fuel cell cathode kinetics: model thin Film  $\text{SrTi}_{1-x}\text{Fe}_{x}\text{O}_{3-\delta}$  mixed conducting oxides—a case study, *Adv. Energy Mater.* 1 (2011) 1184–1191, <https://doi.org/10.1002/aenm.201100164>.
- [21] Z. Shao, S.M. Haile, A high-performance cathode for the next generation of solid-oxide fuel cells, *Mater. Sustain. Energy A Collect. Peer-Rev. Res. Rev. Artic. Nat. Publ. Gr.* 3 (2010) 255–258, [https://doi.org/10.1142/9789814317665\\_0036](https://doi.org/10.1142/9789814317665_0036).
- [22] Y. Chen, S. Yoo, Y. Choi, J.H. Kim, Y. Ding, K. Pei, R. Murphy, Y. Zhang, B. Zhao, W. Zhang, H. Chen, Y. Chen, W. Yuan, C. Yang, M. Liu, A highly active,  $\text{CO}_2$ -tolerant electrode for the oxygen reduction reaction, *Energy Environ. Sci.* 11 (2018) 2458–2466, <https://doi.org/10.1039/c8ee01140k>.
- [23] Y. Chen, S. Yoo, X. Li, D. Ding, K. Pei, D. Chen, Y. Ding, B. Zhao, R. Murphy, B. deGlee, J. Liu, M. Liu, An effective strategy to enhancing tolerance to contaminants poisoning of solid oxide fuel cell cathodes, *Nano Energy* 47 (2018) 474–480, <https://doi.org/10.1016/j.nanoen.2018.03.043>.
- [24] S.P. Jiang, J.P. Zhang, X.G. Zheng, A comparative investigation of chromium deposition at air electrodes of solid oxide fuel cells, *J. Eur. Ceram. Soc.* 22 (2002) 361–373, [https://doi.org/10.1016/S0955-2219\(01\)00280-1](https://doi.org/10.1016/S0955-2219(01)00280-1).
- [25] S.P. Jiang, Y. Zhen, Mechanism of Cr deposition and its application in the development of Cr-tolerant cathodes of solid oxide fuel cells, *Solid State Ion.* 179 (2008) 1459–1464, <https://doi.org/10.1016/j.ssi.2008.01.006>.
- [26] J. Hong, S.J. Heo, A.N. Aphale, B. Hu, P. Singh,  $\text{H}_2\text{O}$  absorption assisted Sr-segregation in strontium nickel oxide based chromium getter and encapsulation with  $\text{SrCO}_3$ , *J. Electrochem. Soc.* 166 (2019) F59, <https://doi.org/10.1149/2.0351902jes>.
- [27] B.-K. Park, R.-H. Song, S.-B. Lee, T.-H. Lim, S.-J. Park, W. Jung, J.-W. Lee, Conformal bi-layered perovskite/spinel coating on a metallic wire network for solid oxide fuel cells via an electrodeposition-based route, *J. Power Sources* 348 (2017) 40–47, <https://doi.org/10.1016/j.jpowsour.2017.02.080>.
- [28] Y. Niu, Y. Zhou, W. Lv, Y. Chen, Y. Zhang, W. Zhang, Z. Luo, N. Kane, Y. Ding, L. Soule, Y. Liu, W. He, M. Liu, Enhancing oxygen reduction activity and Cr tolerance of solid oxide fuel cell cathodes by a multiphase catalyst coating, *Adv. Funct. Mater.* 31 (2021) 1–11, <https://doi.org/10.1002/adfm.202100034>.
- [29] J. Huang, Q. Liu, S.P. Jiang, L. Zhao, N. Ai, X. Wang, Y. Shao, C. Guan, H. Fang, Y. Luo, K. Chen, Promotional role of  $\text{BaCO}_3$  on the chromium-tolerance of  $\text{La}_{0.6}\text{Sr}_{0.4}\text{Co}_{0.2}\text{Fe}_{0.8}\text{O}_{3-\delta}$  cathodes of solid oxide fuel cells, *Appl. Catal. B Environ.* 321 (2023) 122080, <https://doi.org/10.1016/j.apcatb.2022.122080>.
- [30] H.A. Ishfaq, M.Z. Khan, Y.M. Shirke, S. Qamar, A. Hussain, M.T. Mehran, R.-H. Song, M. Saleem, A heuristic approach to boost the performance and Cr poisoning tolerance of solid oxide fuel cell cathode by robust multi-doped ceria coating, *Appl. Catal. B Environ.* 323 (2023) 122178, <https://doi.org/10.1016/j.apcatb.2022.122178>.
- [31] B. Koo, K. Kim, J.K. Kim, H. Kwon, J.W. Han, W.C. Jung, Sr segregation in perovskite oxides: why it happens and how it exists, *Joule* 2 (2018) 1476–1499, <https://doi.org/10.1016/j.joule.2018.07.016>.
- [32] Y. Chen, W. Jung, Z. Cai, J.J. Kim, H.L. Tuller, B. Yildiz, Impact of Sr segregation on the electronic structure and oxygen reduction activity of  $\text{SrTi}_{1-x}\text{Fe}_x\text{O}_3$  surfaces, *Energy Environ. Sci.* 5 (2012) 7979–7988, <https://doi.org/10.1039/C2EE21463F>.
- [33] W. Jung, H.L. Tuller, Investigation of surface Sr segregation in model thin film solid oxide fuel cell perovskite electrodes, *Energy Environ. Sci.* 5 (2012) 5370–5378, <https://doi.org/10.1039/c1ee02762j>.
- [34] G.M. Rupp, A.K. Opitz, A. Nenning, A. Limbeck, J. Fleig, Real-time impedance monitoring of oxygen reduction during surface modification of thin film cathodes, *Nat. Mater.* 16 (2017) 640–645, <https://doi.org/10.1038/nmat4879>.
- [35] E. Mutoro, E.J. Crumlin, M.D. Biegalski, H.M. Christen, Y. Shao-Horn, Enhanced oxygen reduction activity on surface-decorated perovskite thin films for solid oxide fuel cells, *Energy Environ. Sci.* 4 (2011) 3689–3696, <https://doi.org/10.1039/C1EE01245B>.
- [36] C. Argiridis, S. Wagner, W. Meneskou, C. Warnke, T. Damjanovic, G. Borchardt, E. Ivers-Tiffée, Enhancement of oxygen surface exchange kinetics of  $\text{SrTiO}_3$  by alkaline earth metal oxides, *Phys. Chem. Chem. Phys.* 7 (2005) 3523–3525, <https://doi.org/10.1039/B51084A>.
- [37] S.F. Wagner, C. Warnke, W. Meneskou, C. Argiridis, T. Damjanović, G. Borchardt, E. Ivers-Tiffée, Enhancement of oxygen surface kinetics of  $\text{SrTiO}_3$  by alkaline earth metal oxides, *Solid State Ion.* 177 (2006) 1607–1612, <https://doi.org/10.1016/j.ssi.2006.04.026>.
- [38] C. Argiridis, F. Jomard, S.F. Wagner, W. Meneskou, E. Ivers-Tiffée, Study of the oxygen incorporation and diffusion in  $\text{Sr}(\text{Ti}_{0.65}\text{Fe}_{0.35})\text{O}_3$  ceramics, *Solid State Ion.* 192 (2011) 9–11, <https://doi.org/10.1016/j.ssi.2010.02.016>.
- [39] M. Siebenhofer, C. Riedl, A. Nenning, W. Artnar, C. Rameshan, A.K. Opitz, J. Fleig, M. Kubicek, Improving and degrading the oxygen exchange kinetics of  $\text{La}_{0.6}\text{Sr}_{0.4}\text{CoO}_{3-\delta}$  by Sr decoration, *J. Mater. Chem. A* (2023), <https://doi.org/10.1039/D2TA09362F>.
- [40] S.D. Safian, N.I. Abd Malek, Z. Jamil, S.-W. Lee, C.-J. Tseng, N. Osman, Study on the surface segregation of mixed ionic-electronic conductor lanthanum-based perovskite oxide  $\text{La}_{1-x}\text{Sr}_x\text{Co}_{1-y}\text{Fe}_y\text{O}_{3-\delta}$  materials, *Int. J. Energy Res.* 46 (2022) 7101–7117, <https://doi.org/10.1002/er.7733>.
- [41] M. Siebenhofer, C. Riedl, A. Nenning, W. Artnar, C. Rameshan, P. Blaha, J. Fleig, M. Kubicek, Engineering surface dipoles on mixed conducting oxides with ultra-thin oxide decoration layers, *Nat. Commun.* 15 (2024) 1730, <https://doi.org/10.1038/s41467-024-45824-9>.
- [42] C. Nicollet, C. Toparli, G.F. Harrington, T. Defferrriere, B. Yildiz, H.L. Tuller, Acidity of surface-infiltrated binary oxides as a sensitive descriptor of oxygen exchange kinetics in mixed conducting oxides, *Nat. Catal.* 3 (2020) 913–920, <https://doi.org/10.1038/s41929-020-00520-x>.
- [43] H.G. Seo, A. Staerz, D.S. Kim, D. Klotz, C. Nicollet, M. Xu, J.M. LeBeau, H.L. Tuller, Reactivation of chromia poisoned oxygen exchange kinetics in mixed conducting solid oxide fuel cell electrodes by serial infiltration of lithia, *Energy Environ. Sci.* 15 (2022) 4038–4047, <https://doi.org/10.1039/D1EE03975J>.
- [44] H.G. Seo, A. Staerz, D.S. Kim, J.M. LeBeau, H.L. Tuller, Tuning Surface Acidity of Mixed Conducting Electrodes: Recovery of Si-Induced Degradation of Oxygen Exchange Rate and Area Specific Resistance, *Adv. Mater.* 35 (2023) 2208182, <https://doi.org/10.1002/adma.202208182>.
- [45] J.W. Stevenson, T.R. Armstrong, R.D. Carneim, L.R. Pederson, W.J. Weber, Electrochemical Properties of Mixed Conducting Perovskites  $\text{La}_{1-x}\text{M}_x\text{Co}_{1-y}\text{Fe}_y\text{O}_{3-\delta}$  ( $\text{M} = \text{Sr}, \text{Ba}, \text{Ca}$ ), *J. Electrochem. Soc.* 143 (1996) 2722, <https://doi.org/10.1149/1.1837098>.
- [46] B. Koo, H. Kwon, Y. Kim, H.G. Seo, J.W. Han, W. Jung, Enhanced oxygen exchange of perovskite oxide surfaces through strain-driven chemical stabilization, *Energy Environ. Sci.* 11 (2018) 71–77, <https://doi.org/10.1039/c7ee00770a>.
- [47] W. Lee, J.W. Han, Y. Chen, Z. Cai, B. Yildiz, Cation size mismatch and charge interactions drive dopant segregation at the surfaces of manganite perovskites, *J. Am. Chem. Soc.* 135 (2013) 7909–7925, <https://doi.org/10.1021/ja3125349>.
- [48] A. Rothschild, W. Meneskou, H.L. Tuller, E. Ivers-Tiffée, Electronic structure, defect chemistry, and transport properties of  $\text{SrTi}_{1-x}\text{Fe}_x\text{O}_{3-y}$  solid solutions, *Chem. Mater.* 18 (2006) 3651–3659, <https://doi.org/10.1021/cm052803x>.
- [49] T. Zhu, H.E. Troiani, L.V. Mogni, M. Han, S.A. Barnett, Ni-Substituted  $\text{Sr}(\text{Ti},\text{Fe})\text{O}_3$  SOFC anodes: achieving high performance via metal alloy nanoparticle exsolution, *Joule* 2 (2018) 478–496, <https://doi.org/10.1016/j.joule.2018.02.006>.

- [50] A. Nenning, L. Volgger, E. Miller, L.V. Mogni, S. Barnett, J. Fleig, The electrochemical properties of  $\text{Sr}(\text{Ti},\text{Fe})\text{O}_{3-\delta}$  for anodes in solid oxide fuel cells, *J. Electrochim. Soc.* 164 (2017) F364, <https://doi.org/10.1149/2.1271704jes>.
- [51] T. Yang, S.L. Kollasch, J. Grimes, A. Xue, S.A. Barnett,  $(\text{La}_{0.8}\text{Sr}_{0.2})_{0.98}\text{MnO}_3$ - $\delta$ - $\text{Zr}_{0.92}\text{Y}_{0.16}\text{O}_{2-\delta}$ - $\text{PrO}_x$  for oxygen electrode supported solid oxide cells, *Appl. Catal. B Environ.* 306 (2022) 121114, <https://doi.org/10.1016/j.apcatb.2022.121114>.
- [52] N.A. Baharuddin, N.A. Mohd Nazrul Aman, A. Muchtar, M.R. Somalu, A. Abdul Samat, M.I. Aznam, Structural, morphological, and electrochemical behavior of titanium-doped  $\text{SrFe}_{1-x}\text{Ti}_x\text{O}_{3-\delta}$  ( $x = 0.1\text{--}0.5$ ) perovskite as a cobalt-free solid oxide fuel cell cathode, *Ceram. Int.* 45 (2019) 12903–12909, <https://doi.org/10.1016/j.ceramint.2019.03.216>.
- [53] S.W.D. Gourley, T. Or, Z. Chen, Breaking free from cobalt reliance in lithium-ion batteries, *IScience* 23 (2020) 101505, <https://doi.org/10.1016/j.isci.2020.101505>.
- [54] F. Ciucci, Electrical conductivity relaxation measurements: statistical investigations using sensitivity analysis, optimal experimental design and ECRTOOLS, *Solid State Ion.* 239 (2013) 28–40, <https://doi.org/10.1016/j.ssi.2013.03.020>.
- [55] T.H. Wan, M. Saccoccia, C. Chen, F. Ciucci, Influence of the discretization methods on the distribution of relaxation times deconvolution: implementing radial basis functions with DRTtools, *Electrochim. Acta* 184 (2015) 483–499, <https://doi.org/10.1016/j.electacta.2015.09.097>.
- [56] M. Vračar, A. Kuzmin, R. Merkle, J. Purans, E.A. Kotomin, J. Maier, O. Mathon, Jahn-Teller distortion around  $\text{Fe}^{4+}$  in  $\text{Sr}(\text{Fe},\text{Ti}_{1-x})\text{O}_{3-\delta}$  from X-ray absorption spectroscopy, X-ray diffraction, and vibrational spectroscopy, *Phys. Rev. B* 76 (2007) 174107, <https://doi.org/10.1103/PhysRevB.76.174107>.
- [57] E.J. Crumlin, E. Mutoro, W.T. Hong, M.D. Biegalski, H.M. Christen, Z. Liu, H. Bluhm, Y. Shao-Horn, In Situ ambient pressure X-ray photoelectron spectroscopy of cobalt perovskite surfaces under cathodic polarization at high temperatures, *J. Phys. Chem. C* 117 (2013) 16087–16094, <https://doi.org/10.1021/jp4051963>.
- [58] A. Nenning, A.K. Opitz, C. Rameshan, R. Rameshan, R. Blume, M. Hävecker, A. Knop-Gericke, G. Rupprecht, B. Klötzer, J. Fleig, Ambient Pressure XPS study of mixed conducting perovskite-type SOFC cathode and anode materials under well-defined electrochemical polarization, *J. Phys. Chem. C* 120 (2016) 1461–1471, <https://doi.org/10.1021/acs.jpcc.5b08596>.
- [59] C. Yao, H. Zhang, Y. Dong, R. Zhang, J. Meng, F. Meng, Characterization of Ta/W co-doped  $\text{SrFeO}_{3-\delta}$  perovskite as cathode for solid oxide fuel cells, *J. Alloy. Compd.* 797 (2019) 205–212, <https://doi.org/10.1016/j.jallcom.2019.05.096>.
- [60] H. Zhang, K. Xu, F. He, Y. Zhou, K. Sasaki, B. Zhao, Y. Choi, M. Liu, Y. Chen, Surface regulating of a double-perovskite electrode for protonic ceramic fuel cells to enhance oxygen reduction activity and contaminants poisoning tolerance, *Adv. Energy Mater.* 12 (2022) 2200761, <https://doi.org/10.1002/aenm.202200761>.
- [61] T. Maruyama, T. Inoue, T. Akashi, Standard Gibbs energies of formation of  $\text{SrCrO}_4$  and  $\text{Sr}_3\text{Cr}_2\text{O}_8$ , *Mater. Trans. Jim.* 39 (1998) 1158–1161, <https://doi.org/10.2320/matertrans1989.39.1158>.
- [62] C.B. Gopal, S.M. Haile, An electrical conductivity relaxation study of oxygen transport in samarium doped ceria, *J. Mater. Chem. A* 2 (2014) 2405–2417, <https://doi.org/10.1039/c3ta13404k>.
- [63] M.W. den Otter, H.J.M. Bouwmeester, B.A. Boukamp, H. Verweij, Reactor flush time correction in relaxation experiments, *J. Electrochim. Soc.* 148 (2001) J1, <https://doi.org/10.1149/1.1337604>.
- [64] Y. Zhang, F. Yan, B. Hu, C. Xia, M. Yan, Chemical relaxation in porous ionic-electronic conducting materials represented by the distribution of characteristic times, *J. Mater. Chem. A* 8 (2020) 17442–17448, <https://doi.org/10.1039/DOTA05613H>.
- [65] E. Fischer, J.L. Hertz, Measurability of the diffusion and surface exchange coefficients using isotope exchange with thin film and traditional samples, *Solid State Ion.* 218 (2012) 18–24, <https://doi.org/10.1016/j.ssi.2012.05.003>.
- [66] H.G. Seo, D.H. Kim, J. Seo, S.J. Jeong, J. Kim, H.L. Tuller, J.W. Son, W.C. Jung, High-performance and durable fuel cells using Co/Sr-free fluorite-based mixed conducting  $(\text{Pr},\text{Ce})\text{O}_{2-\delta}$  Cathode, *Adv. Energy Mater.* (2022), <https://doi.org/10.1002/aenm.202202101>.
- [67] W. Jung, H.L. Tuller, Investigation of cathode behavior of model thin-film  $\text{SrTi}_{1-x}\text{Fe}_x\text{O}_{3-\delta}$  ( $x=0.35$  and  $0.5$ ) mixed ionic-electronic conducting electrodes, *J. Electrochim. Soc.* 155 (2008) B1194, <https://doi.org/10.1149/1.2976212>.
- [68] R. Merkle, J. Maier, How is oxygen incorporated into oxides? a comprehensive kinetic study of a simple solid-state reaction with  $\text{SrTiO}_3$  as a model material, *Angew. Chem. Int. Ed.* 47 (2008) 3874–3894, <https://doi.org/10.1002/anie.200700987>.
- [69] F. Ciucci, C. Chen, Analysis of electrochemical impedance spectroscopy data using the distribution of relaxation times: a Bayesian and hierarchical Bayesian approach, *Electrochim. Acta* 167 (2015) 439–454, <https://doi.org/10.1016/j.electacta.2015.03.123>.
- [70] Y. Chen, Y. Bu, Y. Zhang, R. Yan, D. Ding, B. Zhao, S. Yoo, D. Dang, R. Hu, C. Yang, M. Liu, A Highly Efficient and robust nanofiber cathode for solid oxide fuel cells, *Adv. Energy Mater.* 7 (2017), <https://doi.org/10.1002/aenm.201601890>.
- [71] L. Liu, A. Corma, Metal catalysts for heterogeneous catalysis: from single atoms to nanoclusters and nanoparticles, *Chem. Rev.* 118 (2018) 4981–5079, <https://doi.org/10.1021/acs.chemrev.7b00776>.
- [72] S.D. Vora, U.S. DOE Office of Fossil Energy Solid Oxide Fuel Cell Program-19th Annual Solid Oxide Fuel Cell (SOFC) Project Review Meeting, 2018.
- [73] H.G. Seo, A. Staerz, G. Dimitrakopoulos, D. Kim, B. Yildiz, H.L. Tuller, Degradation and recovery of solid oxide fuel cell performance by control of cathode surface acidity: case study – impact of Cr followed by Ca infiltration, *J. Power Sources* 558 (2023) 232589, <https://doi.org/10.1016/j.jpowsour.2022.232589>.
- [74] M. Bilton, A.P. Brown, S.J. Milne, Investigating the optimum conditions for the formation of calcium oxide, used for  $\text{CO}_2$  sequestration, by thermal decomposition of calcium acetate, *J. Phys. Conf. Ser.* 371 (2012) 12075, <https://doi.org/10.1088/1742-6596/371/1/012075>.
- [75] R.A. De Souza, Limits to the rate of oxygen transport in mixed-conducting oxides, *J. Mater. Chem. A* 5 (2017) 20334–20350, <https://doi.org/10.1039/c7ta04266c>.